Available online at www.sciencedirect.com
ScienceDirect
International Journal of Heat and Mass Transfer 50 (2007) 2246–2259
International Journal of HEAT and MASS TRANSFER
www.elsevier.com/locate/ijhmt

On vapor bubble formation around heated nanoparticles in liquids

Mathias Dietzel *, Dimos Poulikakos [1]

Laboratory of Thermodynamics in Emerging Technologies, Institute of Energy Technology, Department of Mechanical and Process Engineering, ETH Zurich, 8092 Zurich, Switzerland

Received 6 June 2006; received in revised form 6 October 2006
Available online 2 January 2007

Abstract

The phenomenon of bubble growth around a laser-heated nanoparticle suspended in a carrier liquid is analytically and numerically investigated. The amount of particle coagulation occurring while the carrier fluid is in the liquid phase is estimated by a monodispersed particle coagulation model using three different estimates of increasing accuracy, but also complexity, in determining the characteristic time of vapor formation as the relevant coagulation duration parameter. The effect of the particle on the bubble stability and the bubble dynamics is also demonstrated.

Keywords: Nanoparticles; Colloidal dispersion; Nanobubble formation; Bubble stability; Particle coagulation; Laser irradiation

1. Introduction

The unique thermophysical properties of ultrafine particles in the nanometer-range, exemplified by a significantly reduced melting temperature compared to their bulk counter part [1], are of vivid interest in the engineering science nowadays. The particles are commonly dispersed for technical applications in a carrier liquid to facilitate their transport which in turn requires a separation process once the particles reach their desired location. The latter is a non-trivial task due to the negligibly small buoyancy force (i.e. no particle settling). A method alleviating this difficulty and adding the benefit of simultaneous thermal processing is the use of volatile liquids as solvents evaporated with a heat source after deposition. The deposition and successive heating of these nanoinks has led to innovative manufacturing methods for electrical conducting structures [2–5]. These methods require the control of thermocapillarity, wetting and evaporation under the influence of an external heat source for the liquid phase as well as particle motion, coagulation and coalescence for the dispersed solid phase. The nanoink structure is typically printed with a drop-on-demand (DOD) ink jet device, whereby an extended (e.g. oven) or a local (e.g. laser) heat source is used to evaporate the carrier liquid and to cure the nanoparticles [2,6]. Despite the fact that the heating process is crucial to the quality (e.g. low specific electrical resistance) of the formed structure, most attempts of improvement rely on empiricism as the processes involved are complex and interweaved: the particles are usually sterically stabilized with a thiol-group adsorbed to the particle surface. This stabilization collapses within a certain temperature range (typically $T_{\text{collapse}} = 330$–$430$ K), allowing the particles to coagulate. Vapor bubbles start to form as soon the liquid temperature exceeds local superheating conditions. The particles pose a void, initiating heterogeneous nucleation. However, it is completely unclear whether particle coagulation is mostly embedded in a vapor or a liquid surrounding. In other words, an understanding is missing whether coagulation is faster or slower than the heat-up and the bubble formation phase. This particular question shall be accessed within this work for a setup where the heat is supplied through the absorption of laser light by the particles. A

* Corresponding author. Tel.: +41 44 63 22588; fax: +41 44 63 21176.
E-mail addresses: dietzel@ltnt.iet.mavt.ethz.ch (M. Dietzel), dimos.poulikakos@ethz.ch (D. Poulikakos).
[1] Tel.: +41 44 63 22039; fax: +41 44 63 21176.

0017-9310/$ - see front matter © 2006 Elsevier Ltd. All rights reserved.
doi:10.1016/j.ijheatmasstransfer.2006.10.035

Nomenclature

Latin symbols

c	heat capacity (J kg^{-1} K^{-1})
c_0	particle concentration (–)
$\bar{c}_b$	fluctuation speed (–)
d_b	bubble diameter (m)
d_p	particle diameter (m)
$\overline{D}_{diff}$	diffusion coefficient (–)
$\overline{g}$	transition parameter (–)
h_{lv}	latent heat (J kg^{-1})
k_B	Boltzmann constant (J K^{-1})
$\dot{m}''$	mass flow density (kg m^{-2} s^{-1})
$\overline{N}_p$	number concentration (–)
p	pressure (Pa)
r, R	radial coordinate (m), (–)
R_v	gas constant (J kg^{-1} K^{-1})
s_l	specific liquid entropy (J kg^{-1} K^{-1})
s_v	specific vapor entropy (J kg^{-1} K^{-1})
t	time (s)
T	temperature (K)
v_0	reference velocity (m s^{-1})
v_v	specific vapor volume (m^3 kg^{-1})
w, W	interface velocity (m s^{-1}), (–)

Dimensionless numbers

Ja	Jakob number (–)
LHP*	laser heat parameter (–)
Re_p	Reynolds number (–)
Pr	Prandtl number (–)
We_p	Weber number (–)

Greek symbols

β, $\bar{\beta}$	collision kernel (–)
ε	density parameter (–)
ϕ	bubble parameter (–)
γ, Γ	surface tension (N m^{-1}), (–)
η	dynamic viscosity (kg m^{-1} s^{-1})
κ	interaction parameter (–)
λ	thermal conductivity (W m^{-1} K^{-1})
μ	chemical potential (J kg^{-1})
ϑ	temperature (°C)
ρ	density (kg m^{-3})
τ	time (–)
ξ	contact angle (rad)
Π	pressure (–)
Θ	temperature (–)

Subscripts

0	initial
b	bubble
c	critical
eq	equilibrium
init	initialisation
l	liquid
ML	monolayer
s	static
sat	saturation
SPH	superheat
p	particle
v	vapor

Mathematical operators

D_τ	Lagrangian derivative towards τ
∂_R	partial derivative towards coordinate R

reasonable answer is expected to foster the further progress in the suitable process timing and parameter control.

The degree of particle coagulation as a function of time is estimated with a monodispersed coagulation model available from the literature [7]. The time of vapor formation describing how fast two vapor bubbles developing around two heated neighboring particles meet is used as the relevant characteristic time. This time is derived with three different approaches of increasing complexity: the first simply compares the laser power absorbed by one particle with the energy it takes to heat-up both, the particle and the surrounding liquid, as well as to evaporate the latter. The second estimates the bubble growth with the Mikic solution of the Rayleigh–Plesset equation [8] and the third is based on the well-established vapor bubble growth model of Scriven. This model solves next to the Rayleigh–Plesset equation the one-dimensional energy equation without assuming a thin thermal layer in which evaporation is taking place [9]. Thus, it solves the one-dimensional Navier–Stokes and energy equation in spherical coordinates. However, the laser heat source, the surface tension effect (important for very small bubbles) as well as the influence of the particle on the interfacial energy of the bubble are not considered in Scriven's work. These necessary extensions are included in the present analysis.

The coagulation model is summarized in Section 2; Section 3 contains the derivation of the characteristic time of bubble growth in conjunction with some estimates of how many particles coagulate in the liquid phase. Some aspects about the stability of vapor bubbles forming around heated nanoparticles are addressed in Section 4. Concluding remarks are made in Section 5.

2. Coagulation times

Particle coagulation in a disperse suspension fluid can be approximated with the monodispersed coagulation model suggested by Kruis et al. [7]. The time evolution of the

particle number concentration $\overline{N}_p$ in a dimensionless form reads:

$$D_\tau \overline{N}_p = -\frac{1}{2}\bar{\beta}\overline{N}_p^2, \tag{1}$$

where τ is the time non-dimensionalized with the ratio of a reference velocity v_0 ($v_0 = 5\ \mathrm{m\ s^{-1}}$) and the particle diameter d_{p0} ($d_{p0} = 10 \times 10^{-9}\ \mathrm{m} = 10\ \mathrm{nm}$). The collision kernel $\bar{\beta}$ is the sum of Brownian (perikinetic) and shear-induced (orthokinetic) coagulation:

$$\bar{\beta} = \beta c_0 = (\beta_{\mathrm{Brown}} + \beta_{\mathrm{shear}})c_0, \tag{2}$$

where c_0 is the volumetric particle concentration. Typical nanoparticle suspension liquids have a particle loading of about 1.5% in volume ($c_0 = 0.015$) and 30–40% in weight. Integration of Eq. (1) with a constant overall collision kernel provides:

$$\overline{N}_p = \frac{1}{1 + 0.5\bar{\beta}\tau}, \quad 1 \geqslant \overline{N}_p > 0. \tag{3}$$

The Brownian collision kernel from the continuum to the free molecular regime is for spherical particles [7],

$$\beta_{\mathrm{Brown}} = 48\overline{D}_{\mathrm{diff}}\left[\frac{1}{1+\sqrt{2}\bar{g}} + \overline{D}_{\mathrm{diff}}\frac{4\sqrt{2}}{\bar{c}_b}\right]^{-1} \tag{4}$$

with the diffusion coefficient according to the Stokes–Einstein relation [10]:

$$\overline{D}_{\mathrm{diff}} = \frac{C_{\mathrm{Kn}}}{d_p^2 v_0}\frac{k_B T_p}{3\pi\eta_l}. \tag{5}$$

The correction for kinetic effects C_{Kn} (slip factor) approaches unity in this application [7]. k_B is the Boltzmann constant, T_p the absolute particle temperature (assumed to be the boiling temperature of the carrier fluid toluene, 383 K) and $\eta_{v/l}$ the dynamic viscosity of the carrier fluid (vapor or liquid, $\eta_v = 2.75 \times 10^{-5}\ \mathrm{Pa\,s}$, $\eta_l = 5.6 \times 10^{-4}\ \mathrm{Pa\,s}$). The mean thermal speed $\bar{c}_b$ and transition parameter $\bar{g}$ read:

$$\bar{c}_b = \sqrt{\frac{48}{\pi^2}\frac{k_B T_p}{\rho_p d_p^3 v_0^2}}, \tag{6}$$

$$\bar{g} = \frac{(1+\bar{l})^3 - (1+\bar{l}^2)^{3/2}}{3\bar{l}} - 1, \quad \bar{l} = \frac{8}{\pi}\frac{\overline{D}_{\mathrm{diff}}}{\bar{c}_b} \tag{7}$$

ρ_p is the particle density ($\rho_p = 19\ 300\ \mathrm{kg\ m^{-3}}$).

The shear-induced coagulation kernel in Eq. (2) is approximated with (spherical particle)[11]:

$$\beta_{\mathrm{shear}} = 2.48\dot{\bar{\gamma}}. \tag{8}$$

The local dimensionless shear $\dot{\bar{\gamma}}$ is at most 6×10^{-3} as seen from FEM-simulations for typical nanoink-curing applications [12]. Using the thermophysical properties of toluene respectively gold (particle), one finds the following values of the collision kernels:

$$\beta_{\mathrm{Brown,l}} = 0.09306, \quad \beta_{\mathrm{Brown,v}} = 1.142, \quad \beta_{\mathrm{shear}} = 0.01488. \tag{9}$$

These numbers reflect the common experience that $\beta_{\mathrm{shear}} < \beta_{\mathrm{Brown,l}} < \beta_{\mathrm{Brown,v}}$ for small particles and non-turbulent flow.

Eq. (3) in conjunction with the values of the collision kernels in Eq. (9) allows making a statement about what percentage of the particles are coagulated before a vapor bubble forms if the characteristic bubble formation time is known. The latter is estimated in the next section.

3. Bubble meeting times

The characteristic time τ_c needed for two vapor bubbles developing around neighboring particles heated by absorbed laser light to meet is estimated herein. It is assumed that the particle/bubble configuration keeps its spherical symmetry in light of the small system dimensions (i.e. negligible buoyancy forces potentially leading to bubble lift-off) and the brief time-scales under investigation. The bubble meeting time is defined herein as the time it takes until the vapor bubbles developing around two neighboring particles meet in the middle (assuming a symmetrical growth rate for each particle). The volumetric particle number concentration is defined as

$$c_0 = n_p\frac{\pi}{6}\left(\frac{d_{p0}}{L}\right)^3, \tag{10}$$

n_p is the number of particles in a reference volume of characteristic length L. The average particle center-to-center distance (cubic arrangement) is

$$\Delta l_p = L/\sqrt[3]{n_p} = d_{p0}\sqrt[3]{\frac{\pi/6}{c_0}}. \tag{11}$$

The critical bubble diameter d_{bc} reads therefore in terms of the bubble parameter $\phi = d_b/d_{p0}$ (ratio between the time dependent bubble diameter d_b and the particle diameter, Fig. 1)

$$\phi_c \equiv \phi(\tau_c) = \frac{d_{bc}}{d_{p0}} = \frac{1}{2}\frac{\Delta l_p - d_{p0}}{d_{p0}} = \frac{1}{2}\left(\sqrt[3]{\frac{\pi/6}{c_0}} - 1\right) \tag{12}$$

with $c_0 = 0.015$ it is $\phi_c = 1.13$.

Model 1: comparison between required heat and power input

A first estimate of the bubble meeting time sums the energy required to heat-up the particle and the liquid, evaporate the liquid and to perform the corresponding volumetric and interfacial work to generate a bubble:

$$Q_{\mathrm{req}} = (\rho_p V_p c_p + \rho_v V_{bc} c_l)\Delta T + \rho_v V_{bc} h_{lv} + (p_l - p_v)V_{bc} + \gamma_{lv}A_{bc} + \gamma\cos(\xi_s)A_p, \tag{13}$$

and compares this heat with the power provided by the laser. In Eq. (13), c_p and c_l are the particle and the liquid heat capacity, V_p is the particle volume and V_{bc} is the liquid

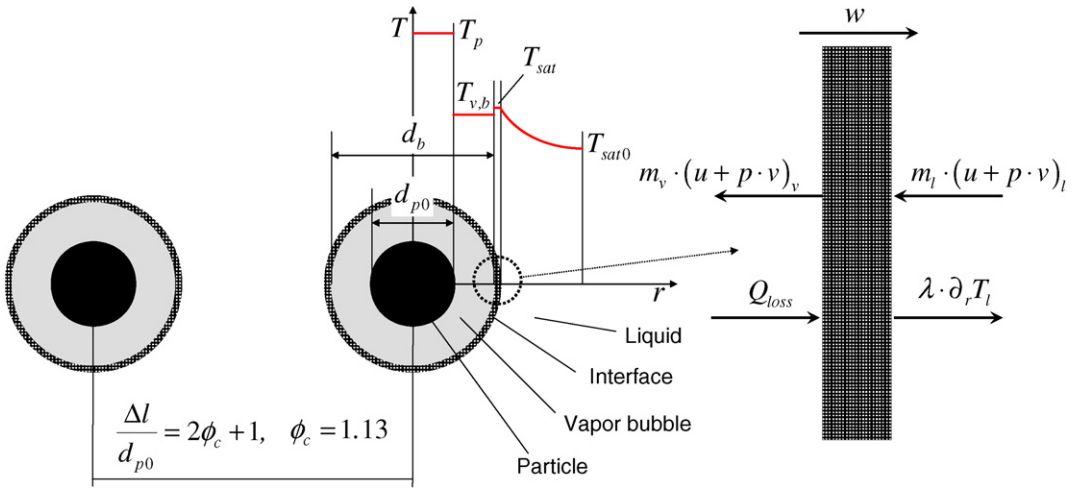

Fig. 1. Nanoparticle, vapor bubble and travelling evaporation layer.

volume to be evaporated. ΔT is the corresponding temperature difference during the heat-up phase, ρ_v is the vapor density and h_{lv} is the latent heat of evaporation. p_l and p_v are the liquid and the vapor pressure respectively. γ is the liquid–vapor interfacial energy with the bubble surface area A_{bc}. The last term in Eq. (13) considers the difference in interfacial energy of the particle surface with area A_p if the particle is either surrounded by a vapor or a liquid phase using the Young–Dupré equation:

$$\gamma_{vp} - \gamma_{lp} = \gamma \cos(\xi_s), \tag{14}$$

γ_{vp} and γ_{lp} is the interfacial energy of the vapor-particle and the liquid-particle interface. ξ_s is the static contact angle which approaches zero in this application (the carrier liquid wets the particles well). If the pressure difference in Eq. (13) is in addition replaced by Laplace's equation (simplified form of Eq. (A.7), i.e. neglecting the viscous stress and recoiling pressure term) one finds,

$$Q_{req} = (\rho_p V_p c_p + \rho_v V_{bc} c_l)\Delta T + \rho_v V_{bc} h_{lv} + \gamma\left(A_{bc} + A_p - \frac{4}{d_{bc}} V_{bc}\right). \tag{15}$$

The surface areas and the evaporated volume can be expressed with

$$A_p = \pi d_{p0}^2, \quad A_{bc} = \pi d_{p0}^2 \phi_c^2, \quad V_{bc} = \frac{\pi}{6} d_{p0}^3 (\phi_c^3 - 1). \tag{16}$$

Introducing the dimensionless temperature

$$\Theta = \frac{T}{T_\infty}, \tag{17}$$

with $T_\infty = 383$ K as the (reference) saturation temperature for a flat surface (which is here the boiling temperature of toluene) and the particle Weber number,

$$We_p = \frac{\rho_l v_0^2 d_{p0}}{\gamma_{lv}} = 7.76 \times 10^{-3} \tag{18}$$

expression (15) can be rearranged to

$$\frac{Q_{req}}{\rho_l c_l T_\infty \pi d_{p0}^3} = \frac{1}{6}\left[\frac{\rho_p}{\rho_l}\frac{c_p}{c_l} + \frac{\rho_v}{\rho_l}(\phi_c^3 - 1)\right]\Delta\Theta + \frac{1}{6}\frac{\rho_v}{\rho_l}\frac{h_{lv}}{c_l T_\infty}(\phi_c^3 - 1) + \frac{1}{We_p}\frac{\gamma}{\gamma_{lv}}\frac{v_0^2}{c_l T_\infty}\left(\phi_c^2 + 1 - \frac{2}{3}\frac{\phi_c^3 - 1}{\phi_c}\right) \tag{19}$$

ρ_l is the liquid density.

The laser power absorbed by the particle in a dimensionless form is

$$\frac{P_{laser}}{\rho_l c_l v_0 T_\infty \pi d_{p0}^2} = \frac{\dot{I}_0''}{\rho_l c_l v_0 T_\infty} \equiv \mathrm{LHP}^*, \tag{20}$$

where $\dot{I}_0''$ is the area-specific laser intensity irradiating on the particle surface A_p. The laser power varies in typical nanoink-curing applications between 0.05 and 0.4 W and the focal diameter between 10 and 50 μm; the absorption depth was estimated to 1 μm [2,3]. Here we use a laser power of 0.17 W and a focal diameter of 30 μm. This leads for a volumetric particle concentration of $c_0 = 0.015$ to an average dimensionless laser intensity per particle of $\mathrm{LHP}^* = 1.55 \times 10^{-2}$.

The time to heat the particle and the liquid to the boiling temperature can be approximated with the ratio between the first term on the right hand side (RHS) of Eqs. (19) and (20) (assuming negligible temperature gradients in the liquid)

$$\tau_{ML2boil,LHP} = \frac{1}{6}\frac{1}{\mathrm{LHP}^*}\left[\frac{\rho_p}{\rho_l}\frac{c_p}{c_l} + \frac{\rho_v}{\rho_l}(\phi_c^3 - 1)\right]\Delta\Theta_B, \tag{21}$$

where $\Delta\Theta_B$ is the relevant temperature difference to be estimated in the following:

The nanoparticles in realistic applications are protected by a monolayer of a thiol-compound to prevent early coagulation. This monolayer is temperature sensitive and

collapses reversible above a critical temperature range of 330–430 K (dependent on the specific compound used). Here we set this temperature to $T_{ML} = 338$ K ($\Theta_{ML} = 0.88$). The relevant temperature difference to overcome is therefore $\Delta\Theta_B = 1 - \Theta_{ML} = 0.12$. With this, the initial heat-up phase is according to Eq. (21) $\tau_{ML2boil,LHP} = 2.162$.

Correspondingly, the approximate time to heat-up the particle as well as the liquid from the boiling temperature to the bubble formation temperature (superheating) and to generate the bubble reads (ratio between Eqs. (19) and (20)):

$$\tau_{boil2c,LHP} = \frac{1}{6}\frac{1}{LHP^*}\frac{h_{lv}}{c_l T_\infty}\left[\left(\frac{\rho_p}{\rho_l}\frac{c_p}{c_l} + \frac{\rho_v}{\rho_l}\left(\phi_c^3 - 1\right)\right)Ja + \frac{\rho_v}{\rho_l}\left(\phi_c^3 - 1\right) + 2\frac{\Gamma}{We_p}\frac{v_0^2}{h_{lv}}\left(\phi_c^2 + \frac{2}{\phi_c} + 3\right)\right]. \quad (22)$$

The terms involving the Jakob number (Ja) consider the energy required to heat the particle, respectively the liquid from the boiling to the superheating temperature. The second term accounts for the latent heat of evaporation whereas the last incorporates the interfacial and volumetric work of bubble formation with $\Gamma \equiv \gamma/\gamma_{lv}$. The Jakob number in Eq. (22) is defined as

$$Ja = \frac{c_l \Delta T}{h_{lv}}, \quad (23)$$

ΔT is the superheat required to maintain an equilibrium bubble and is depending on the bubble size and the surface tension. The latter is herein allowed to vary and estimated with the following equation:

$$\Gamma \equiv \frac{\gamma}{\gamma_{lv}} = \left(1 - \frac{\Delta T}{T_{crit} - T_\infty}\right)^2 \left\{1 + \left(\frac{\gamma_{lp}}{\gamma_{lv}} - 1\right)\exp[-\kappa(\phi - 1)]\right\}. \quad (24)$$

T_{crit} is the critical temperature, γ_{lv} is the liquid–vapor (without the presence of the particle) and γ_{lp} is the liquid-particle interfacial tension, approximated herein with $\gamma_{lp} = 0.18\,\gamma_{lv}$. Eq. (24) combines in an empirical fashion Macleod's well-known formula (first brackets) for the temperature dependence of surface tension [13] with an expression suggested by Kofman et al. [14] for the dependence of surface tension on the particle-to-interface distance. The latter dependence can be understood as follows: the interfacial tension must be that of a solid–liquid interface if the distance is zero. On the other hand, the interfacial tension must approach that of an isolated vapor–liquid interface (without the particle influence) for very large distances. The Kofman-formula postulates now a continuous (here exponential) variation between both limiting values for distances in the range of intermolecular forces from the solid surface, affecting the vapor–liquid interfacial tension. Considering the very small bubble sizes, respectively vapor thicknesses in the present work, this effect has to be accounted for herein. In Eq. (24), κ is an empirical constant quantifying the particle interaction range, i.e. the range of the intermolecular forces from the particle surface affecting the surface tension of the bubble interface.

The required superheat to maintain an equilibrium bubble of size ϕ is given by [15]:

$$\Delta T = \frac{p_\infty - p_{sat|\Delta T}}{\rho_l R_v \ln\left[p_\infty / p_{sat|\Delta T}\left(1 + \frac{4}{We_p}\frac{\Gamma}{\phi}\right)\right]} - T_\infty, \quad (25)$$

where R_v is the mass-specific gas constant. The saturation pressure $p_{sat|\Delta T}$ is taken for toluene from [16]. An iterative procedure using Eqs. (24) and (25) and the saturation curve provides finally (for $\kappa = 10^{-1}$) $\Delta T_{|\phi=1} = 89.4$ K, $\Delta T_{|\phi=1.13} = 87.8$ K and an averaged Jakob number of $Ja = 0.37$. Evaluating Eq. (22) results in $\tau_{boil2c,LHP} = 4.523$.

Summing up the results of Eqs. (21) and (22) yields an approximate bubble meeting time of $\tau_{c,LHP} = 6.685$. With Eq. (3) this would imply that the particle number concentration $\overline{N}_p$ is reduced to only $\overline{N}_p = 0.995$ before vapor formation start.

The time to heat-up the particle and the liquid from Θ_{ML} to the superheated state $\Theta_{eq,10\ nm} = 1.23$ (i.e. the equilibrium temperature of a 10 nm bubble) where bubble formation starts is

$$\tau_{ML2SPH,LHP} = \tau_{ML2boil,LHP}\frac{\Delta\Theta_{SPH}}{\Delta\Theta_B} = 6.306, \quad (\Delta\Theta_{SPH} = \Theta_{eq,10\ nm} - \Theta_{ML}). \quad (26)$$

The actual bubble growth time is thus anticipated to be very brief compared to the heating period ($\tau_{growth,LHP} = 0.379$). In the following, more refined models to estimate the bubble meeting time are discussed.

Model 2: Mikic-solution

There exist numerous works in the literature on bubble growth in an initially uniformly superheated liquid. In general three stages of bubble growth can be distinguished: growth controlled by surface tension, liquid inertia and thermal diffusion. The Rayleigh solution predicts bubble growth proportional to time for the inertia dominated region, whereas bubble growth in the region dominated by thermal diffusion occurs proportional to the square root of time. The latter was derived by [17,18] through the assumption of a thin thermal boundary layer as it is particularly fulfilled for large superheats, and by [9], where the thermal diffusion equation was solved. In Ref. [8] an expression for the bubble radius evolution was obtained valid throughout the inertia- and diffusion controlled domain. This solution interpolates between the limiting solutions for inertia-, respectively diffusion controlled growth and reads:

$$R^+ = \frac{2}{3}\left[(t^+ + 1)^{3/2} - (t^+)^{3/2} - 1\right], \quad (27)$$

where the scaled variables are given by

$$R^+ = \frac{1}{2}\phi\frac{d_{p0}A}{B^2}, \quad t^+ = \tau\frac{d_{p0}}{v_0}\left(\frac{A}{B}\right)^2, \quad A^2 = \frac{2}{3}\frac{\rho_v}{\rho_l}\frac{h_{lv}^2}{c_l T_\infty}Ja, \quad B = \frac{\rho_l}{\rho_v}Ja\sqrt{\frac{12}{\pi}\frac{v_0 d_{p0}}{Re_p Pr}}, \quad (28)$$

Re_p and Pr are the particle Reynolds and Prandtl number, respectively. These are defined as

$$Re_p = \frac{\rho_l v_0 d_p}{\eta_l} = 7.74 \times 10^{-2}, \quad Pr = \frac{c_l \eta_l}{\lambda_l} = 7.38. \tag{29}$$

For the critical bubble parameter it is

$$R_c^+ = 2.15 \times 10^{-6}, \quad A_c = 9.32\sqrt{\mathrm{J/kg}}, \quad B_c = 0.157\ \mathrm{m}/\sqrt{\mathrm{s}}. \tag{30}$$

Solving for the time $t^+_{\mathrm{growth,Mikic}}$ with $R^+_{|t^+_{\mathrm{growth,Mikic}}} \equiv R_c^+$ results in $t^+_{\mathrm{growth,Mikic}} = 2.15 \times 10^{-6}$ or $\tau_{\mathrm{growth,Mikic}} = 0.3035$. The corresponding bubble meeting time is thus $\tau_{\mathrm{c,Mikic}} = \tau_{\mathrm{ML2SPH,LHP}} + \tau_{\mathrm{growth,Mikic}} = 6.6095$. With Eq. (3) and according to the current estimate, the particle number concentration drops again only to $\overline{N}_p = 0.995$ (0.5% reduction) before bubble formation start. This estimate is however highly sensitive to the specific collision kernel employed in Eq. (3). The maximum possible collision kernel for this application is obtained if the influence of the particle concentration on the collision kernel (Eq. (2)) is neglected, i.e. c_0 is set to unity. This leads to an estimate of $\overline{N}_p = 0.737$.

Model 3: extended Scriven-model (see Appendix A)

The shortcomings of both models in the present application are either the complete disregard of inertial and diffusive transport effects (Eq. (22)) or the focus on these two mechanisms only, in combination with the assumption of an initially uniformly superheated liquid. A more detailed bubble formation model is used to improve the accuracy of the prediction which solves numerically the one-dimensional momentum (i.e. the Rayleigh–Plesset equation) and energy equation in spherical coordinates, whereby the formulation of [9] is adopted. However, since surface tension effects are particularly important for small droplets, the basic approach is merged with formulations of [19,20] to also incorporate surface tension. The main difference to the previous work is a variable surface tension as a function of bubble size and temperature according to Eq. (24) as well as the inclusion of a nanoparticle in the bubble interior and heated through the absorption of laser light.

The model is detailed in Appendix A and computes the bubble parameter ϕ, the dimensionless interface velocity W and the particle temperature Θ_p with a standard fourth order Runge-Kutta scheme in time (time step $\Delta\tau = [10^{-7},10^{-3}]$). The liquid temperature field is solved with a second order finite difference scheme in space and either the implicite Euler (uniformly preheated liquid) or a fully implicite scheme (laser-heated particle) are used for the time integration. The temperature grid employs spherical, non-constant grid spacings in R expressed with the following coordinate transformation function:

$$x = a + \sqrt{c^2 - (\zeta - b)^2}; \quad x = \frac{R - R_0}{R_{\max} - R_0}; \quad b = 1 - a; \ c = \sqrt{2a(a-1)+1} \tag{31}$$

The numerical grid in ζ is equally spaced with $\Delta\zeta = 2.5 \times 10^{-3}$. The grid parameter a is set to $a = 1.1$ herein. This provides with $R_{\max} = 50$ a variable grid spacing for R in the range $\Delta R \approx [10^{-1},6 \times 10^{0}]$. The thermal Neumann boundary condition (A.26) at the bubble interface is incorporated with the help of a fictitious interior node to keep second order accuracy at the interface node [21]. It was ensured that the solutions obtained are time step and grid size independent.

Fig. 2 shows the characteristic bubble growth quantities (i.e. bubble diameter, interface velocity and liquid pressure difference $\Delta p = p_{l,d_b} - p_{l,\infty}$, Eq. (A.6)) for water at ambient conditions ($p_\infty = 1$ atm), superheated with $\Delta T = 15$K and containing no particle in the interior. The thermophysical properties of water, in particular the saturation curve, are taken from [22]. The initial (equilibrium) bubble diameter is $d_{b0} = 4.25\mu$m. The initial disturbance to initiate the bubble growth is solely the numerical inaccuracy between determining the initial bubble diameter as a function of the given superheat and computing the vapor pressure for a given temperature. However, it could be seen from additional simulations (not shown for brevity) that adding and increasing the initial temperature disturbances shortens the bubble growth waiting period as discussed in [20]. The characteristics found are in excellent agreement with data published by [23] on the same problem which serves as a verification case.

Fig. 3 plots the bubble growth time $\tau_{\mathrm{growth,SPH}}$ (disregarding the heating phase of the particle and the liquid to superheated conditions) as a function of the initially uniform liquid superheat for different values of the interaction parameter κ (Eq. (24)), i.e. the simulations use a variable surface tension depending on the temperature and on the interface location. Heat transfer from the liquid to the

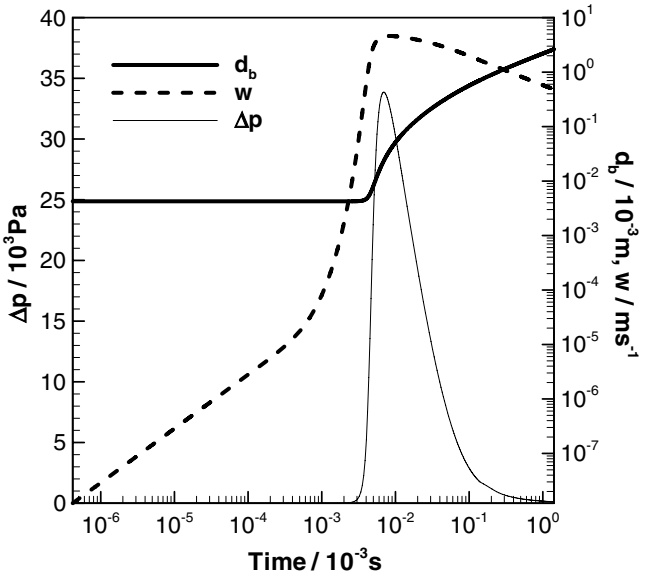

Fig. 2. Bubble growth characteristics for water with ambient conditions, $p_\infty = 1$ atm, $\Delta T_{\mathrm{sup}} = 15$ K.

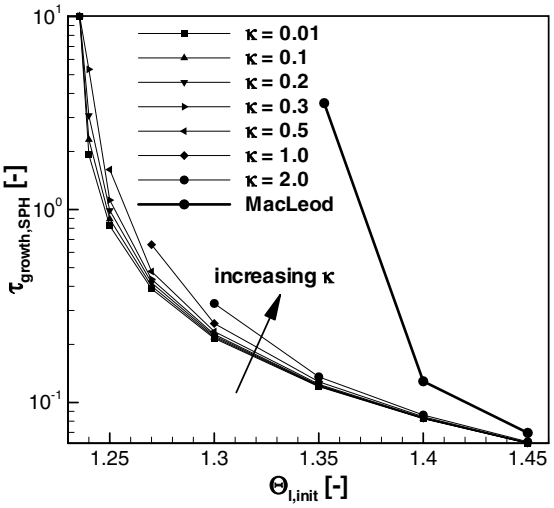

Fig. 3. Bubble growth time $\tau_{\text{growth,SPH}}$ vs. initial uniform liquid superheat as a function of the interaction parameter κ for a particle diameter of $d_{\text{p0}} = 10$ nm.

particle is assumed by convection (neglecting the influence of the vapor phase thickness) and radiation. A Nusselt number (related to the vapor heat conductivity) of 7.42 is employed. The latter value was derived in accordance with the kinetic theory of gases [24]. The initial bubble radius is equal to the particle diameter, $d_{\text{p0}} = 10$ nm, and the thermophysical properties of toluene are used. All growth times are equal or below $\tau_{\text{growth,SPH}} = 10.0$, whereby the slowest bubble growth occurs if the initial liquid temperature equals the equilibrium temperature of a 10 nm vapor bubble, $\Theta_{\text{eq,10 nm}} = 1.23$. Increasing the superheat lowers rapidly the growth time to a value below $\tau_{\text{growth,SPH}} = 0.1$ at an initial liquid temperature of $\Theta_{\text{l,init}} = 1.45$. The influence of the interaction strength κ is generally weak except for values above $\kappa = 0.5$ where it prevents the formation and growth of a vapor bubble for smaller values of $\Theta_{\text{l, init}}$. This behavior is further reasoned in Section 4. The bold line in Fig. 3 uses a variation of surface tension with temperature only (Macleod's formula, first bracket in Eq. (24)). It requires a higher liquid superheat to maintain and grow a 10 nm bubble ($\Theta_{\text{l,init}} \geqslant 1.35 = \Theta_{\text{eq,10 nm,Macleod}}$) and thus the bubble growth time stays well below $\tau_{\text{growth,SPH}} = 10.0$. Note in this context that a 10nm bubble in toluene requires theoretically supercritical conditions if a surface tension correction in the form of Eq. (24) is not introduced. In summary, Fig. 3 emphasizes that the bubble growth time should be very short after the conditions for bubble formation are attained compared to the heat-up time.

At last we want to discuss the case when the particle is embedded in a cool liquid and heated e.g. by laser light absorption. Heat transfer from the particle to the liquid is assumed by conduction (taking the thickness of the vapor layer into account) and radiation; the vapor film is assumed to have negligible heat capacity. The simulations for this case were undertaken with $R_{\max} = 0.565$ ($=0.5\phi_c$) for the temperature solution, i.e. the symmetry boundary condition of a horizontal temperature gradient was applied at this location. The spacing of the numerical grid is $\Delta\zeta = 14.5 \times 10^{-3}$, which provides a variable grid spacing for R in the range $\Delta R \approx [10^{-4}, 7 \times 10^{-3}]$. The model predicts a particle/liquid heating time to superheated conditions of $\tau_{\text{ML2SPH,LHP}} = 8.73$ which is markedly longer than the analytical approximation made in Eq. (26) for the same laser intensity ($\text{LHP}^* = 1.55 \times 10^{-2}$). This is due to the fact that the simulation considers the liquid mass of volume V_{bc} as a heat sink whereas Eq. (26) uses the vapor mass of the same volume only, which is by the factor $\rho_{\text{v}}/\rho_{\text{l}}$ less. Using

$$\tilde{\tau}_{\text{ML2SPH,LHP}} = \frac{1}{6}\frac{1}{\text{LHP}^*}\left[\frac{\rho_{\text{p}}}{\rho_{\text{l}}}\frac{c_{\text{p}}}{c_{\text{l}}} + \left(\phi_{\text{c}}^3 - 1\right)\right]\Delta\Theta_{\text{SPH}}, \quad \Delta\Theta_{\text{SPH}} = 0.35, \tag{32}$$

for the heat-up phase provides indeed $\tilde{\tau}_{\text{ML2SPH,LHP}} = 7.971$. Thus, non-linear effects are weak during the heating phase and the model predicts that a steady-state temperature gradient is established at the particle surface after only $\Delta\tau_{\text{non-linear}} = 5 \times 10^{-3}$. Temperature gradients in the liquid are generally small thereafter and the liquid temperature is quasi-uniform for all times. The start of bubble formation is assumed to occur always at the particle surface, hence decisive for bubble formation is the smallest activation energy not the smallest Laplace pressure (promoting larger bubbles, see Section 4).

Fig. 4 plots the bubble growth time vs. the particle interaction parameter κ for the two laser intensities $\text{LHP}^* = \{0.0155, 0.155\}$ and for either conductive (case c1) or infinite (i.e. the interface temperature equals the particle temperature, case c2) heat transfer between the particle and the bubble interface. The initial heating period was neglected and all simulations start with an initial temperature of $\Theta_{\text{l, init}} = 1.23$. The model predicts a bubble growth time

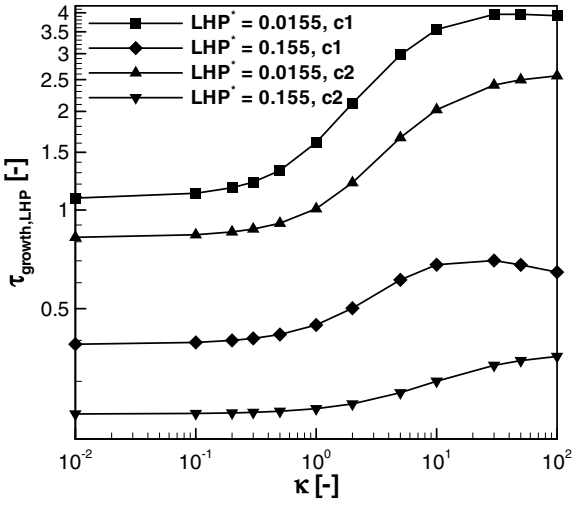

Fig. 4. Bubble growth time $\tau_{\text{growth, LHP}}$ vs. particle interaction parameter κ for different laser intensities LHP*. Either conductive (case c1) or infinite (i.e. interface temperature equals particle temperature, case c2) heat transfer was assumed.

between $0.75 < \tau_{\text{growth,LHP}} < 4.0$ for $\text{LHP}^* = 1.55 \times 10^{-2}$ and $0.24 < \tau_{\text{growth,LHP}} < 0.7$ for $\text{LHP}^* = 1.55 \times 10^{-1}$. Lowering the heat transfer from the particle to the interface prolongs as expected the growth time. The range of $\tau_{\text{growth,LHP}}$ for low laser intensity suggests that the other two estimates significantly underestimated the growth time between two and thirteen times. Increasing the particle interaction parameter for both laser intensities and heat transfer assumptions leads to a progressive increase in the bubble growth time until $\kappa = 10.0$, whereby the strong rise is more pronounced for the low laser intensity. A further increase of κ flattens the slope of the growth time for both laser intensities. The case with a finite (conductive) heat transfer assumption reaches a peak in growth time at about $\kappa = 30.0$.

To explain the general shape of the curves shown in Fig. 4, one can plot the Kofman-part of the surface tension Eq. (24),

$$\Gamma_K = \Gamma\left(1 - \frac{\Delta T}{T_{\text{crit}} - T_\infty}\right)^{-2} = \left\{1 + \left(\frac{\gamma_{\text{lp}}}{\gamma_{\text{lv}}} - 1\right)\exp[-\kappa(\phi - 1)]\right\} \tag{33}$$

in the bubble parameter range of interest ($\phi = [1, \phi_c]$), Fig. 5. The surface tension evolution itself until the bubble has grown to the critical diameter and the change of this surface tension evolution with κ is relatively small for small κ-values ($\kappa = 0.01 - 1.0$). Contrary, the evolution and the change of this evolution is significant for larger, intermediate κ-values, explaining the strong non-linear behavior seen in the bubble growth time in Fig. 4. However, the surface tension remains constant after an initial steep increase for very large κ-values ($\kappa \geqslant 100.0$) which reasons the flattening of the curve in Fig. 4 for large particle interaction parameters (the part of the bubble growth where the surface tension is not constant becomes increasingly small compared to the part where the surface tension is constant for large κ-values). The general rise in surface tension within the bubble parameter range of interest if κ is increased explains the generally longer bubble growth times for these cases observed in Fig. 4 since it becomes increasingly difficult to grow the bubble. As a summary of Figs. 4 and 5, the variation of the particle interaction parameter κ has the largest impact on the bubble growth time if κ is in the order or one order larger than the bubble parameter, causing the largest change of the bubble surface tension variation throughout the bubble growth.

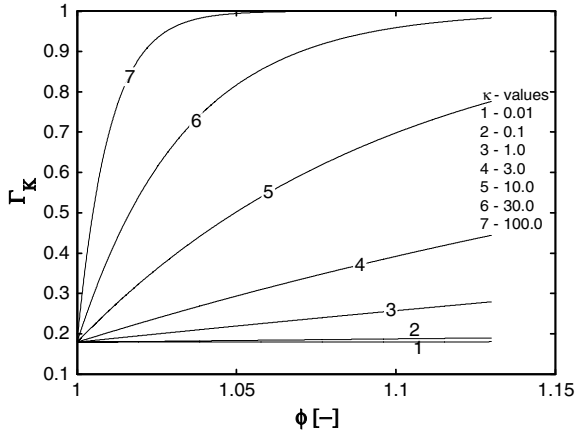

Fig. 5. Surface tension evolution vs. bubble parameter according to Eq. (33) as a function of particle interaction parameter κ.

Computing the overall bubble meeting time $\tau_{\text{c,LHP}}$ with the previously computed time to reach superheated conditions (beginning with the collapse of the monolayer), $\tau_{\text{ML2SPH,LHP}}$, and the bubble growth time and inserting the result in Eq. (3) leads to the particle number concentration at the critical time. Fig. 6 plots the particle number concentration at the start of vapor formation vs. the particle interaction parameter for both heat transfer assumption and for a laser intensity of $\text{LHP}^* = 1.55 \times 10^{-2}$. The particle number concentration is reduced only about 1% if the coagulation kernel computed with Eq. (2) is used and is practically independent of the specific value of the particle interaction parameter. Since a monodispersed coagulation model is known to underpredict the extent of particle coagulation compared to a fully polydispersed model [10], Fig. 6 shows also the particle number concentration at the critical time using the maximal possible collision kernel in this application, i.e. a kernel independent of the particle concentration ($c_0 = 1.0$) to visualize the sensitivity. Here, the particle number concentration is reduced more than 35% and the particle interaction parameter has a significant effect. Both heat transfer assumptions yield similar predictions for low values of the particle interaction parameter. However, the extent of particle coagulation is stronger

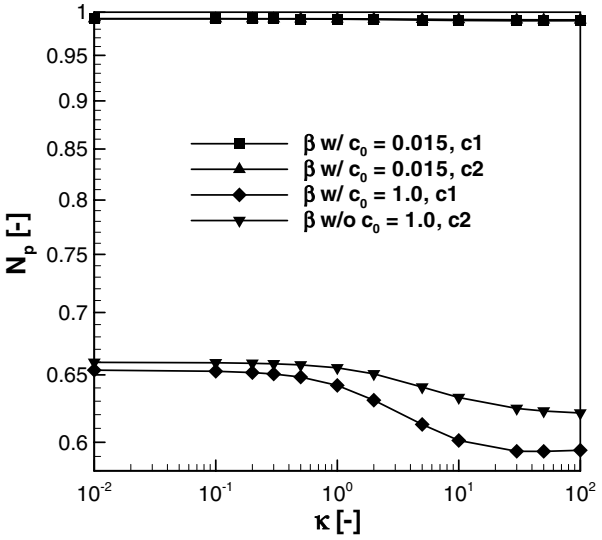

Fig. 6. Particle number concentration at $\tau_{\text{c,LHP}}$ vs. particle interaction parameter κ for $\text{LHP}^* = 1.55 \times 10^{-2}$, both heat transfer assumptions (case c1: conductive heat transfer; case c2: interface temperature equals particle temperature) and a collision kernel dependent (w/c_0) or independent (w/o c_0) of the particle concentration.

increased in the case of conductive heat transfer and high values of κ.

Hence, the particle interaction parameter has an effect only for large collision kernels. In any case, the first estimate of the particle coagulation upon bubble meeting time is proven to be a good approximation, despite the partly large differences in the bubble growth time prediction. Thus, only a small amount of the particles can be expected to coagulate in the liquid phase. The majority coagulates after the evaporation of the carrier liquid. In fact, this is desired from a technical stand-point since the risk of liquid enclosures between coagulated particles is with this unlikely.

Up to now we have assumed that the particle diameter does not change during the heating phase $\tau_{\mathrm{ML2SPH,LHP}}$, i.e. the start of bubble formation was always at $\Theta_{\mathrm{eq,10\ nm}} = 1.23$. This is an approximation since the particles coagulate during this period and change their diameter due to mass conservation according to (assuming immediate full coalescence):

$$d_{\mathrm{p}} = d_{\mathrm{p0}} \overline{N}_{\mathrm{p}}^{-1/3}. \tag{34}$$

Fig. 7 shows the evolution of the relative particle diameter $d_{\mathrm{p}}/d_{\mathrm{p0}}$ vs. time during the heating period along with the particle temperature and the theoretical bubble equilibrium temperature for a bubble diameter equal to the current particle diameter d_{p}. It is assumed that the heating is linear ($d_\tau \Theta = 0.0443$, Eq. (32)) and unaffected by the coagulation process. The collision kernel is assumed to be constant with $\bar{\beta} = 0.10794$, which is the largest possible collision kernel (again neglecting the influence of the particle concentration) to obtain the upper estimate. Bubble formation occurs when the two temperature curves intersect, at $d_{\mathrm{p}}/d_{\mathrm{p0}} = 1.1244$ and $\tau_{\mathrm{ML2SPH,LHP,coag}} = 7.8$ (Fig. 7). This is only marginally smaller than the time needed to reach superheated conditions for an initial bubble diameter of $d_{\mathrm{p}} = d_{\mathrm{p0}} = 10$ nm. Note that the (herein overestimated) collision kernel becomes in general smaller with increasing particle size (smaller particle diffusion coefficient), prolonging the coagulation process and further reducing the difference. In addition, the bubble growth rate is decreasing for increasing initial bubble diameters so that the overall bubble meeting time we are interested in will remain relatively unaffected by the coagulation process.

The next assumption made so far is that the temperature profiles of two adjacent particles interact, i.e. a zero-valued temperature gradient was imposed at the radial position $R = \frac{1}{2}\phi_{\mathrm{c}}$ since ϕ_{c} marks the middle between two neighboring particles. However, this effect does not occur for dilute particle suspension liquids and the consequently large temperature gradient in the liquid at the particle, respectively at the bubble interface once it is formed, will have a strong effect on the dynamics of the problem.

Fig. 8 plots the bubble parameter vs. time for a sole particle heated with a laser intensity of $\mathrm{LHP}^* = 1.55$ (which is hundred times more than in standard applications), starting from an initial temperature of $\Theta_{\mathrm{l,init}} = \Theta_{\mathrm{ML}} = 0.88$. The bubble parameter evolution appears to be usual at first. However, strong oscillations are revealed if one takes a closer look to the interfacial velocity just before major bubble growth starts (inset of Fig. 8). These oscillations are due to the large temperature gradient within the liquid and the corresponding large diffusive heat removal: the bubble starts growing as soon as the particle reaches the required amount of superheat to maintain a bubble equal to the particle diameter but it directly collapses again because the surrounding liquid is too cold at the new interface location after growing to sustain the required Laplace pressure (the convective interfacial motion is faster than the diffusive heat transport). This phenomenon repeats itself in a progressive fashion (as the particle temperature and with it the liquid superheat right at the particle surface after a collapse is constantly increased) until the steep temperature gradient in the liquid is sufficiently reduced due to heat diffusion. These oscillations have a similar origin as acoustical cavitations experimentally observed at hot wires

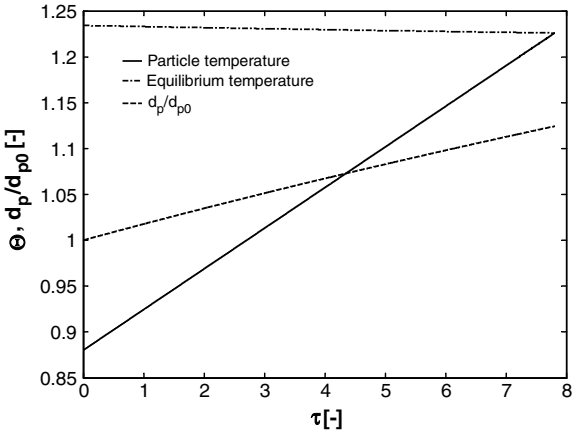

Fig. 7. Particle temperature, equilibrium temperature of bubble with size d_{p} and relative particle diameter $d_{\mathrm{p}}/d_{\mathrm{p0}}$ vs. time.

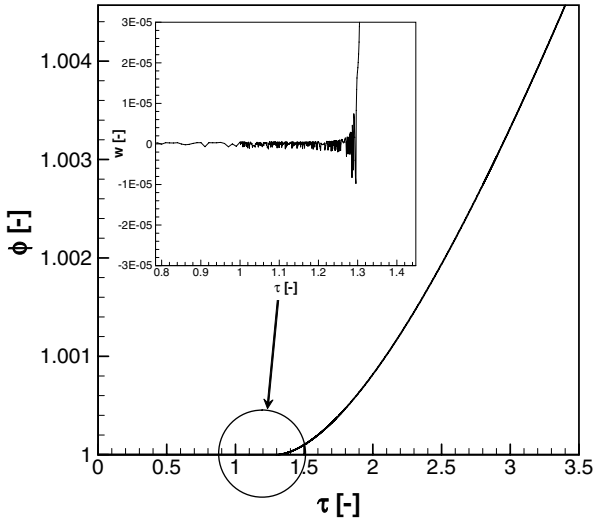

Fig. 8. Bubble parameter and interface velocity (inset) vs. time for $\mathrm{LHP}^* = 1.55$ and sole particle arrangement.

[25]. They can be expected to occur only for very small bubbles which are unaffected by buoyancy and keep the assumed spherical symmetry, like in the current problem. Using lower laser intensities markedly increase the heating period and an efficient solution with the current simulation program was not possible.

4. Stability of nanobubbles surrounding spherical particles

In this section we will discuss some general aspects related to the stability of a vapor bubble surrounding a nanoparticle. Fig. 9 plots the required superheat to maintain an equilibrium bubble of size ϕ_{eq} for different values of the particle interaction parameter κ. The graph is based on an iterative evaluation of Eqs. (24) and (25). Generally, the calculated superheat is very high since the Laplace pressure is very high for nanometer-sized bubbles (in the order of 112 bar).

The case where the particle has no effect on the surface tension of the vapor-liquid interface is practically identically to the case with the largest κ-value ($\kappa = 10^2$) shown in Fig. 9, except in the direct vicinity to the particle ($\phi = 1$) where the no-interaction-case intersects with the ordinate at $\Theta = 1.35$ (not shown), compared to $\Theta = 1.23$ for all cases governed by Eq. (24). The curve is shifted to lower superheats for long-range interaction (small κ-values, case 1–4), whereby the general trend of a monotonic exponential decay is maintained. However, the plots showing the short-range interaction cases (large κ-values, case 6–12) have a maximum at values of the bubble parameter between 1 and 2. This has certain implications on the stability of the nanobubbles as will be discussed below.

The Gibbs free energy of a system containing a solid particle suspended in a superheated liquid reads:

$$G_1 = m_p\mu_p^\infty + m\mu_l^\infty + \gamma_{lp}A_p, \tag{35}$$

m_p is the particle mass with the mass specific chemical potential μ_p^∞. $m = m_v + m_l$ is the sum of the liquid mass to be evaporated, m_v, and the liquid mass which remains liquid, m_l. The total fluid mass has in the initial state the mass specific liquid chemical potential μ_l^∞. A system of the same superheat T_{SPH} and containing next to the particle also a vapor bubble surrounding the particle has the Gibbs free energy of

$$G_2 = m_p\mu_p^\infty + m_v u_v + m_l u_l + m_v\frac{p_l}{\rho_v} + m_l\frac{p_l}{\rho_l} - T_{SPH}(m_v s_v + m_l s_l) + \gamma A_b + \gamma_{vp}A_p, \tag{36}$$

u_v and u_l are the mass specific internal energies of the vapor and the liquid phase, respectively. s_v and s_l are the mass specific entropies of each phase. Note that the pressure in the fourth term on the RHS has to be the liquid pressure since the vapor expansion is against the liquid pressure not against the vapor pressure. Rearranging provides:

$$\begin{aligned} G_2 &= m_p\mu_p^\infty + m_v\left(u_v + \frac{p_v}{\rho_v} - T_{SPH}s_v\right) \\ &\quad + m_l\left(u_l + \frac{p_l}{\rho_l} - T_{SPH}s_l\right) + m_v\left(\frac{p_l}{\rho_v} - \frac{p_v}{\rho_v}\right) + \gamma A_b + \gamma_{vp}A_p \\ &= m_p\mu_p^\infty + m_v\mu_v^\infty + m_l\mu_l^\infty + m_v\left(\frac{p_l}{\rho_v} - \frac{p_v}{\rho_v}\right) + \gamma A_b + \gamma_{vp}A_p, \end{aligned} \tag{37}$$

μ_v^∞ is the mass specific chemical potential of the (extensive) vapor phase. Subtracting Eq. (35) from (37) and using $m_v = \rho_v V_b$ reads:

$$\Delta G_{2-1} = \rho_v V_b(\mu_v^\infty - \mu_l^\infty) + (p_l - p_v)V_b + \gamma A_b + (\gamma_{vp} - \gamma_{lp})A_p. \tag{38}$$

Inserting the Laplace and the Young–Dupré equation as in the derivation of Eq. (15):

$$\Delta G_{2-1} = \rho_v V_b(\mu_v^\infty - \mu_l^\infty) + \gamma\left[A_b - \frac{4}{d_b}V_b + \cos(\xi_s)A_p\right]. \tag{39}$$

Using Eq. (16) and $\Gamma = \gamma/\gamma_{lv}$ (Eq. (24)) and rearranging provides

$$\frac{\Delta G_{2-1}}{\pi d_{p0}^2\gamma_{lv}} = \Delta\overline{G} = \frac{\rho_v d_{p0}}{6\gamma_{lv}}(\phi^3 - 1)(\mu_v^\infty - \mu_l^\infty) + \frac{\Gamma}{3}\left(\phi^2 + \frac{2}{\phi}\right) + \cos(\xi_s). \tag{40}$$

The Gibbs–Duhem equation for an extensive vapor phase reads

$$d\mu_v^\infty = \frac{dp_v}{\rho_v} - s_v dT \tag{41}$$

Employing the ideal gas law:

$$\rho_v = \frac{p_v}{R_v T_{SPH}}, \tag{42}$$

and isothermal conditions leads after integration of Eq. (41) to

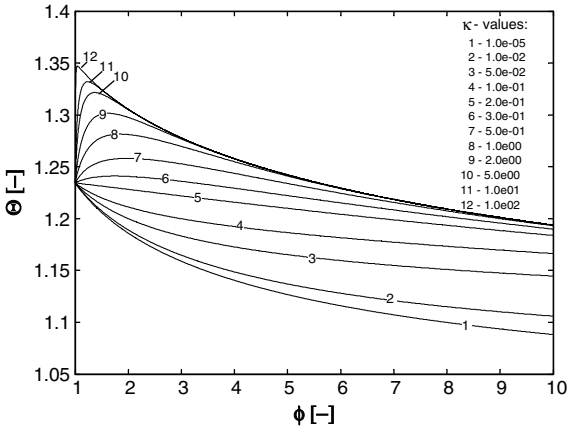

Fig. 9. Superheat at equilibrium vs. bubble size as a function of particle interaction parameter.

$$\mu_{\mathrm{v}}^{\infty} = \mu_{v0}^{\infty} + R_{\mathrm{v}} T_{\mathrm{SPH}} \ln \frac{p_{\mathrm{v}}}{p_{\infty}}. \tag{43}$$

Defining

$$\mu_{v0}^{\infty} - \mu_{\mathrm{l}}^{\infty} = -R_{\mathrm{v}} T_{\mathrm{SPH}} \ln \frac{p_{\mathrm{v,\,eq}}}{p_{\infty}}, \tag{44}$$

and using the ideal gas law and the Laplace equation to express the vapor density in Eq. (40) gives for $p_{\mathrm{l}} \equiv p_{\infty}$

$$\begin{aligned} \Delta\overline{G} &= \frac{p_{\infty} d_{\mathrm{p}}}{6\gamma_{\mathrm{lv}}} \psi(\phi^3 - 1)[\ln(\psi) - \ln(\psi_{\mathrm{eq}})] \\ &\quad + \frac{\Gamma}{3}\left(\phi^2 + \frac{2}{\phi}\right) + \cos(\xi_{\mathrm{s}}) \\ \psi &= \frac{p_{\mathrm{v}}}{p_{\infty}} = 1 + \frac{\rho_{\mathrm{l}} v_0^2}{p_{\infty}} \frac{4}{We_{\mathrm{p}}} \frac{\Gamma}{\phi}. \end{aligned} \tag{45}$$

The expression in the square brackets invokes the change of the chemical potential due to a variation in vapor pressure, assuming extensive phases. The term proportional to the square of ϕ is the equilibrium value for a pure bubble [15], corrected for the presence of the particle (term reciprocal to ϕ). Eq. (45) provides the variation of the bubble Gibbs energy at constant temperature. This temperature is the equilibrium value computed with Eqs. (24) and (25), hence it is $\Delta\overline{G} = f(\phi, \phi_{\mathrm{eq}})$.

Fig. 10 shows the Gibbs energy evolution of the vapor bubble with a variation of the bubble parameter (x-axis) and as a function of the equilibrium bubble parameter (y-axis) according to Eq. (45). Fig. 10a uses $\kappa = 10^{-5}$ whereas in Fig. 10b the value $\kappa = 2 \times 10^{0}$ is employed. The static contact angle is for both cases $\xi_{\mathrm{s}} = 40°$. The Gibbs energy field for the first case is qualitatively identical to the one found for a regular vapor bubble without a particle, i.e. the Gibbs energy has a local maximum at the corresponding equilibrium bubble parameter (unstable equilibrium). The case with the large κ-value behaves however completely different. Equilibrium conditions can only be found in a narrow range of the bubble parameter ($1.5 \leqslant \phi_{\mathrm{eq}} \leqslant 4.0$); the bubble will collapse immediately after it has been formed for all other values. This can be correlated with the findings of Fig. 9: an equilibrium condition is only possible if the bubble parameter exceeds the value of the local maximum, i.e. after the superheat decays exponentially with a further increase of the bubble parameter. Thus, the superheat shown in Fig. 9 does not reflect an equilibrium condition for small bubble parameters and short-range particle interaction parameters. This is rooted in the derivation of Eq. (25), which skips the variation of surface tension in the Gibbs–Duhem equation for the vapor phase. The complete form reads:

$$\mathrm{d}\mu_{\mathrm{v}} = \frac{\mathrm{d}p}{\rho_{\mathrm{v}}} - s_{\mathrm{v}}\mathrm{d}T - \frac{6}{d_{\mathrm{p0}}} \frac{\phi^2}{\phi^3 - 1} \frac{\mathrm{d}\gamma}{\rho_{\mathrm{v}}} \tag{46}$$

$\mathrm{d}\mu_{\mathrm{v}}$ is the variation of the vapor chemical potential and $\mathrm{d}\gamma$ is the variation of the surface tension. The latter is only a function of the bubble parameter which is in turn correlated to the pressure with Laplace's equation (neglecting the flux terms in Eq. (A.7)) since isothermal variations of the chemical potential are considered. With the ideal gas law one can write:

$$\mathrm{d}\mu_{\mathrm{v}} = R_{\mathrm{v}} T \left(1 - \frac{6\gamma_{\mathrm{lv}}}{d_{\mathrm{p0}}} \frac{d_{\phi}\Gamma}{d_{\phi}p} \frac{\phi^2}{\phi^3 - 1}\right) \frac{\mathrm{d}p}{p}. \tag{47}$$

The Laplace equation provides:

$$\frac{d_{\mathrm{p0}}}{6\gamma_{\mathrm{lv}}} \frac{d_{\phi}p}{d_{\phi}\Gamma} = \frac{2}{3\phi}\left(1 - \frac{1}{\phi}\frac{\Gamma}{d_{\phi}\Gamma}\right) \tag{48}$$

Eq. (47) can be transformed to

$$\mathrm{d}\mu_{\mathrm{v}} = R_{\mathrm{v}} T \left[1 - \frac{3}{2}\frac{\phi^3}{\phi^3 - 1}\left(1 - \frac{1}{\phi}\frac{\Gamma}{d_{\phi}\Gamma}\right)^{-1}\right] \frac{\mathrm{d}p}{p}. \tag{49}$$

The stability behavior of a vapor bubble containing a particle is qualitatively similar to that of a pure vapor bubble if the term in the brackets equals a constant $\bar{c}$. A surface tension function which conforms to this restriction can be derived to

$$\Gamma = \frac{\Gamma_{|\phi=1}}{(1-\bar{q})^{(\bar{q}-1)/3}}\left[\phi(\phi^3 - \bar{q})^{(\bar{q}-1)/3}\right], \quad \bar{q} = \frac{1-\bar{c}}{5/2 - \bar{c}} \tag{50}$$

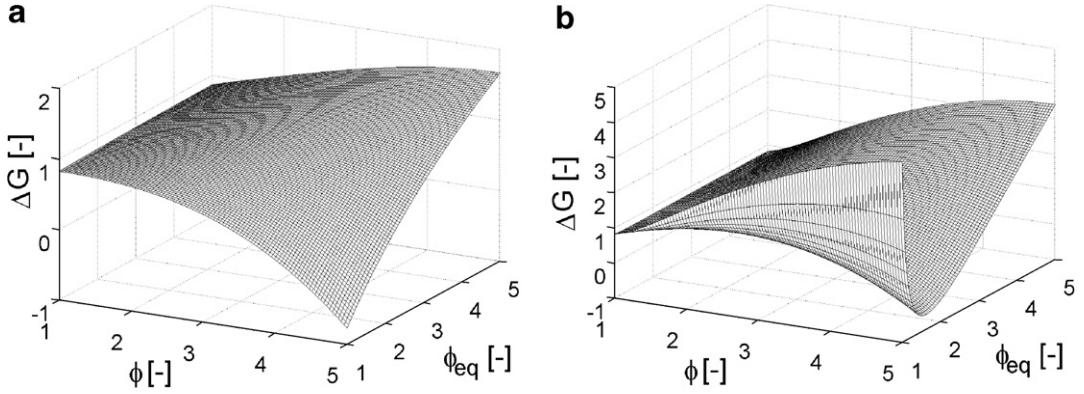

Fig. 10. Variation of Gibbs energy for vapor bubble around nanoparticle (a) $\kappa = 10^{-5}$, (b) $\kappa = 2 \times 10^{0}$.

Eq. (50) dictates the dependence of the surface tension on ϕ (i.e. the distance of the liquid–vapor interface to the particle) in case the particle–bubble system shall have qualitatively the same stability behavior as a pure vapor bubble.

Inserting Eq. (24) into (49) yields:

$$\mathrm{d}\mu_\mathrm{v} = R_\mathrm{v}T\left\{1-\frac{3}{2}\frac{\phi^3}{\phi^3-1}\left[1+\frac{1}{\kappa\phi}\frac{1+\Gamma_1\exp[-\kappa(\phi-1)]}{\Gamma_1\exp[-\kappa(\phi-1)]}\right]^{-1}\right\}\frac{\mathrm{d}p}{p},$$
$$\Gamma_1 = \frac{\gamma_\mathrm{lp}}{\gamma_\mathrm{lv}} - 1. \tag{51}$$

The term in the curly braces approaches unity for $\kappa \to 0$ (long-range interaction) and the variation of surface tension with the bubble parameter has no effect on the bubble stability. However, for $\kappa \to \infty$ (short-range interaction) it is

$$\mathrm{d}\mu_\mathrm{v} = R_\mathrm{v}T\left\{1-\frac{3}{2}\frac{\phi^3}{\phi^3-1}\right\}\frac{\mathrm{d}p}{p}. \tag{52}$$

Here, the term in the braces is not constant and the stability of the particle–bubble system differs from the pure vapor bubble system as observed in Fig. 10b.

The change of the Gibbs energy during the formation of a bubble at thermodynamic equilibrium conditions,

$$\Delta\overline{G}_\mathrm{eq} = \frac{\Gamma}{3}\left(\phi_\mathrm{eq}^2 + \frac{2}{\phi_\mathrm{eq}}\right) + \cos(\xi_\mathrm{s}) \tag{53}$$

is usually positive, i.e. bubble formation requires an activation energy. However, for sufficiently hydrophobic particle surfaces (large ξ_s), the Gibbs energy change is negative and the vapor bubble is in a stable thermodynamic equilibrium. The limiting case is

$$\cos(\xi_\mathrm{s}) = -\Gamma_{|\phi=1} \equiv -\Gamma_1, \tag{54}$$

which provides for the present case a wetting angle of $\xi_\mathrm{s} = 100°$. Also it has to be noted that the formation of an equilibrium vapor bubble around a nanoparticle requires usually higher activation energy than a corresponding pure vapor bubble since in most cases

$$\Delta\overline{G}_\mathrm{eq,purebubble} = \frac{\Gamma}{3}\phi_\mathrm{eq}^2 < \frac{\Gamma}{3}\left(\phi_\mathrm{eq}^2 + \frac{2}{\phi_\mathrm{eq}}\right) + \cos(\xi_\mathrm{s}) = \Delta\overline{G}_\mathrm{eq,w/ptl}. \tag{55}$$

However, the condition changes again for sufficient hydrophobic surface, i.e. for

$$\cos(\xi_\mathrm{s}) < -\frac{2}{3}\frac{\Gamma}{\phi_\mathrm{eq}}. \tag{56}$$

This is commonly experienced during bubble formation at particles enclosing gas pockets on their (rough) surface which degrade the wettability.

5. Conclusions

This work computed the characteristic time of bubble formation around a heated nanoparticle in a liquid and used this time to estimate the extent of particle coagulation in the liquid phase. Three models of increasing complexity were used to approximate the bubble meeting time and a continuous monodispersed particle coagulation model was used to judge the amount of particle coagulation in the liquid phase. The simple models were seen to overpredict the bubble growth rate but since the overall bubble meeting time (heat-up and growth) is relatively short compared to the characteristic particle coagulation time, all models predict that only about 1% of the particles coagulate in the liquid phase for a monodispersed coagulation kernel making liquid enclosures during the curing of nanoparticle ink unlikely.

The extent of particle coagulation is practically independent of the particle interaction parameter, quantifying the interaction range in which the particle affects the interfacial energy of the bubble. However, the monodispersed collision kernel is known to be an underprediction compared to a full polydispersed model. A sensitivity analysis using the theoretically largest possible collision kernel (setting the particle concentration to unity) revealed that the particle number concentration is decreased more than 35% in this case. In addition, the effect of the particle interaction parameter can be more than 5% for this case and is hence significant for large collision kernels. This underpins the importance of deriving a particle collision kernel explicitly valid in a phase changing carrier fluid to make accurate quantitative predictions possible.

It was seen that the particle coagulation itself (potentially accelerating the onset of vapor formation) does not have a crucial influence on the extent of particle coagulation whereas a low particle concentration leads initially to a continuous growth and collapse of the bubble.

It was shown that particles with a large interaction parameter slightly hinder evaporation in weakly superheated liquids and widely change the stability behavior of the vapor bubbles surrounding them.

Appendix A

The model used herein is based on the derivations made in [9,19,20]. It solves numerically the one-dimensional mass, momentum and energy equation, considers surface tension and mass flux effects at the interface and incorporates the presence of the heated nanoparticle. Mass conservation at the bubble interface dictates [9]:

$$\dot{m}'' = \rho_\mathrm{l}(w_\mathrm{i} - w_{\mathrm{l},d_\mathrm{b}}), \tag{A.1}$$

where w_i is the interface velocity, ρ_l is the liquid density and $w_{\mathrm{l},d_\mathrm{b}}$ is the liquid velocity at the interface. The evaporating area-specific mass flux $\dot{m}''$ is according to the kinetic theory of gases [26]:

$$\dot{m}'' = (p_\mathrm{sat} - p_\mathrm{v})/\sqrt{2\pi R_\mathrm{v}T_{\mathrm{l},d_\mathrm{b}}}, \tag{A.2}$$

p_v is the vapor pressure inside the bubble and $T_{\mathrm{l},d_\mathrm{b}}$ is the liquid temperature at the vapor–liquid interface. However, preliminary simulations showed that the numerical system

containing Eq. (A.2) is numerically 'stiff' and therefore cumbersome to solve, which is a direct consequence of the almost constant vapor density inside the bubble. If set constant, relation (A.2) can be replaced with

$$\dot{m}'' = \rho_v w_i, \tag{A.3}$$

where ρ_v is the vapor density. Combining Eqs. (A.1) and (A.3) provides for the radial liquid velocity at the interface:

$$w_{l,d_b} = \varepsilon w_i. \tag{A.4}$$

The density parameter is defined as

$$\varepsilon = 1 - \frac{\rho_v}{\rho_l} \tag{A.5}$$

The liquid velocity has to satisfy the one-dimensional momentum equation (extended or modified Rayleigh equation [9]), which can be brought with $w \equiv w_i$ into the following form

$$d_b \dot{w} + 3w^2 = \frac{2}{\varepsilon\rho_l}(p_{l,d_b} - p_{l,\infty}) \tag{A.6}$$

Here, η_l is the liquid dynamic viscosity, $p_{l,\infty}$ is the liquid pressure far away from the bubble and p_{l,d_b} is the liquid pressure right at the vapor–liquid interface.

A momentum balance (i.e. Laplace's equation) at the interface provides for the latter [20,27,28]:

$$p_{l,d_b} = p_v - \frac{4\gamma}{d_b} - 8\varepsilon\eta_l \frac{w}{d_b} + \frac{\varepsilon}{\rho_v}(\dot{m}'')^2. \tag{A.7}$$

The bubble vapor pressure is approximated with [15]:

$$p_v \approx p_{sat|T_{l,d_b}} \exp\left(-\frac{4}{\rho_l R_v T_{l,d_b}} \frac{\gamma}{d_b}\right). \tag{A.8}$$

The assumption of a spherical symmetric flow made in the derivation of Eq. (A.6) is strictly speaking not valid for a bubble developing around a particle neighbored by other particles. Eq. (A.6) will therefore only serve as a good approximation if the interaction between the neighboring flow fields can be considered to be weak, or, if the velocities are generally small.

The energy equation for the liquid in spherical symmetric coordinates reads:

$$D_t T_l = \frac{\lambda}{\rho_l c_l}\left(\partial_r^2 T_l + \frac{2}{r}\partial_r T_l\right) + \dot{Q}'''_{rad,l,loss} \tag{A.9}$$

$\dot{Q}'''_{rad,l,loss}$ is the heat absorbed by the liquid from the irradiative heat loss generated by the particle. With the law of Lambert–Beer it is

$$\dot{Q}'''_{rad,l,loss} = 2a_{th}\sigma_B\left(T_p^4 - T_{l,d_b}^4\right)\exp[-a_{th}(2r - d_b)] \tag{A.10}$$

where $a_{th} = \hat{a}_{th}/d_{p0}$ is the (low frequency) absorption coefficient empirically set to $a_{th} = 10^6 m^{-1}$. σ_B is the Stefan–Boltzmann-constant ($\sigma_B = 5.67 \times 10^{-8}\ W/m^2\ K^4$) and T_{l,d_b} the liquid temperature at the interface. An energy balance around the particle and the vapor phase provides as a boundary condition for Eq. (A.9) at the interface:

$$\partial_r T_{l|d_b} = \frac{1}{\lambda}\left(\dot{m}'' h_{lv} + \dot{\gamma} - \frac{\dot{Q}_{loss}}{\pi d_b^2}\right). \tag{A.11}$$

The energy loss $\dot{Q}_{loss}$ coming from the heated particle has to be calculated with the energy equation for the particle (disregarding phase change or expansion):

$$\frac{1}{6}\rho_p c_p d_{p0} \dot{T}_p = \dot{I}''_o - \frac{\dot{Q}_{loss}}{\pi d_{p0}^2}, \tag{A.12}$$

$\dot{I}''_0$ is the source term due to laser irradiation with an area-specific heat flux. The heat loss to the liquid can be expressed with

$$\frac{\dot{Q}_{loss}}{\pi d_{p0}^2} = \sigma_B\left(T_p^4 - T_{l,d_b}^4\right) + \frac{\dot{Q}_{loss,cond}}{\pi d_{p0}^2}. \tag{A.13}$$

The first term on the RHS is the loss due to thermal radiation and the second is the loss due to conduction. The latter is defined as

$$\begin{aligned} \frac{\dot{Q}_{loss,cond}}{\pi d_{p0}^2} &= -\lambda_l \partial_r T_{l|\phi=1}, \ \phi = 1 \\ \frac{\dot{Q}_{loss,cond}}{\pi d_{p0}^2} &= -2\lambda_v \frac{T_{l|\phi} - T_p}{d_b - d_{p0}}, \ \phi > 1 \end{aligned} \tag{A.14}$$

The following dimensionless time, temperature, pressure and radial velocity are introduced.

$$\tau = t\frac{v_0}{d_{p0}}, \quad \Theta = \frac{T}{T_\infty}, \quad \Pi = \frac{p}{\rho_l v_0^2}, \quad W = \frac{w_i}{v_0} \tag{A.15}$$

The governing equations change with this to

$$\dot{\phi} = 2\,W \tag{A.16}$$

$$\frac{\dot{m}''}{\rho_l v_0} = \frac{\rho_v}{\rho_l} W \tag{A.17}$$

$$\begin{aligned} \dot{W} = {} & \frac{2}{\varepsilon\phi}\left(\Pi_v - \frac{4}{We_p}\frac{\Gamma}{\gamma_{lv}}\frac{1}{\phi} - \Pi_{l,\infty}\right) \\ & + \frac{\rho_l}{\rho_v}\frac{2}{\phi}\left(\frac{\dot{m}''}{\rho_l v_0}\right)^2 - 3\frac{W^2}{\phi} - \frac{16}{Re_p}\frac{W}{\phi^2} \end{aligned} \tag{A.18}$$

$$\Pi_{l,d_b} = \frac{p_{l,d_b}}{\rho_l v_0^2} = \Pi_v - \frac{4}{We_p}\frac{\Gamma}{\gamma_{lv}}\frac{1}{\phi} - \varepsilon\frac{8}{Re_p}\frac{W}{\phi} + \varepsilon\frac{\rho_l}{\rho_v}\left(\frac{\dot{m}''}{\rho_l v_0}\right)^2 \tag{A.19}$$

$$\Pi_v = \Pi_{sat,\Theta_{l,\phi}} \exp\left(-\frac{v_0^2}{R_v T_\infty}\frac{4}{We_p}\frac{\Gamma}{\phi\Theta_{l,\phi}}\right) \tag{A.20}$$

$$\dot{\Theta}_p = 6\frac{\rho_l}{\rho_p}\frac{c_l}{c_p}\left[\mathrm{LHP}^* - \dot{\bar{Q}}_{loss}\right] \tag{A.21}$$

$$\begin{aligned} \dot{\bar{Q}}_{loss} &= \frac{\dot{Q}_{loss}}{\rho_l c_l v_0 T_\infty \pi d_{p0}^2} \\ &= \frac{\sigma_B T_\infty^3}{\rho_l c_l v_0}\left(\Theta_p^4 - \Theta_{l,\phi}^4\right) + \frac{\dot{Q}_{loss,cond}}{\rho_l c_l v_0 T_\infty \pi d_{p0}^2} \end{aligned} \tag{A.22}$$

$$\frac{\dot{Q}_{\mathrm{loss,cond}}}{\rho_\mathrm{l} c_\mathrm{l} v_0 T_\infty \pi d_{\mathrm{p0}}^2} = -\frac{\partial_R \Theta_{\mathrm{l}|\phi=1}}{Re_\mathrm{p} Pr}, \quad \phi = 1$$

$$\frac{\dot{Q}_{\mathrm{loss,cond}}}{\rho_\mathrm{l} c_\mathrm{l} v_0 T_\infty \pi d_{\mathrm{p0}}^2} = -\frac{2}{Re_\mathrm{p} Pr}\frac{\lambda_\mathrm{v}}{\lambda_\mathrm{l}}\frac{\Theta_{\mathrm{l}|\phi} - \Theta_\mathrm{p}}{\phi - 1}, \quad \phi > 1 \tag{A.23}$$

$$D_\tau \dot{\Theta}_\mathrm{l} = \frac{1}{Re_\mathrm{p} Pr}\left(\partial_R^2 \Theta_\mathrm{l} + \frac{2}{R}\partial_R \Theta_\mathrm{l}\right) + \dot{\overline{Q}}_{\mathrm{rad,l,loss}} \tag{A.24}$$

$$\dot{\overline{Q}}_{\mathrm{rad,l,loss}} = \frac{\dot{Q}''_{\mathrm{rad,l,loss}}}{\rho_\mathrm{l} c_\mathrm{l} T_\infty v_0 / d_{\mathrm{p0}}} = 2\hat{a}_{\mathrm{th}}\frac{\sigma_\mathrm{B} T_\infty^3}{\rho_\mathrm{l} c_\mathrm{l} v_0}\left(\Theta_\mathrm{p}^4 - \Theta_{\mathrm{l},\phi}^4\right) \times \exp[-\hat{a}_{\mathrm{th}}(2R - \phi)] \tag{A.25}$$

$$\partial_R \Theta_{\mathrm{l},\phi} = Re_\mathrm{p} Pr\left(\frac{\dot{m}''}{\rho_\mathrm{l} v_0}\frac{h_\mathrm{lv}}{c_\mathrm{l} T_\infty} + \frac{v_0^2}{c_\mathrm{l} T_\infty}\frac{\dot{I}}{We_\mathrm{p}} - \frac{\dot{\overline{Q}}_{\mathrm{loss}}}{\phi^2}\right). \tag{A.26}$$

References

[1] P. Buffat, J.P. Borel, Size effect on the melting temperature of gold particles, Phys. Rev. A 13 (1975) 2287–2297.

[2] N.R. Bieri, J. Chung, S.E. Haferl, D. Poulikakos, C.P. Grigoropoulos, Microstructuring by printing and laser curing of nanoparticle solutions, Appl. Phys. Lett. 82 (2003) 3529–3531.

[3] N.R. Bieri, J. Chung, D. Poulikakos, C.P. Grigoropoulos, Manufacturing of nanoscale thickness gold lines by laser curing of a discretely deposited nanoparticle suspension, Superlattice. Microstruct. 35 (2004) 437–444.

[4] J. Chung, N.R. Bieri, S. Ko, C.P. Grigoropoulos, D. Poulikakos, In-tandem deposition and sintering of printed gold nanoparticle inks induced by continuous Gaussian laser irradiation, Appl. Phys. A Mater. 79 (2004) 1259–1261.

[5] T.Y. Choi, D. Poulikakos, C.P. Grigoropoulos, Fountain-pen-based laser microstructuring with gold nanoparticle inks, Appl. Phys. Lett. 85 (2004) 13–15.

[6] S.B. Fuller, E.J. Wilhelm, J.A. Jacobson, Ink-jet printed nanoparticle microelectromechanical systems, J. Microelectromech. Syst. 11 (2002) 54–60.

[7] F.E. Kruis, K.A. Kusters, S.E. Pratsinis, B. Scarlett, A simple-model for the evolution of the characteristics of aggregate particles undergoing coagulation and sintering, Aerosol Sci. Technol. 19 (1993) 514–526.

[8] B.B. Mikic, W.M. Rohsenow, P. Griffith, On bubble growth rates, Int. J. Heat Mass Transfer. 13 (1970) 657–665.

[9] L.E. Scriven, On the dynamics of phase growth, Chem. Eng. Sci. 10 (1959) 1–13.

[10] S.K. Friedlander, Smoke, Dust and Haze, second ed., Oxford University Press, Los Angeles, 2000, pp. 33.

[11] G. Barthelmes, S.E. Pratsinis, H. Buggisch, Particle size distributions and viscosity of suspensions undergoing shear-induced coagulation and fragmentation, Chem. Eng. Sci. 58 (2003) 2893–2902.

[12] M. Dietzel, D. Poulikakos, Laser-induced motion in nanoparticle suspension droplets on a surface, Phys. Fluid 17 (2005) 102106.

[13] R.H. Fowler, A tentative statistical theory of Macleod's equation for surface tension, and the parachor, Proc. Roy. Soc. Lond. A Math. A159 (1937) 229–246.

[14] R. Kofman, P. Cheyssac, A. Aouaj, Y. Lereah, G. Deutscher, T. Bendavid, J.M. Penisson, A. Bourret, Surface melting enhanced by curvature effects, Surf. Sci. 303 (1994) 231–246.

[15] V.P. Carey, Statistical Thermodynamics and Microscale Thermophysics, Cambridge University Press, Melbourne, 1999, pp. 357–359.

[16] R.D. Goodwin, Toluene thermophysical properties from 178-K to 800-K at pressures to 1000-bar, J. Phys. Chem. Ref. Data 18 (1989) 1565–1636.

[17] M.S. Plesset, S.A. Zwick, The growth of vapor bubbles in superheated liquids, J. Appl. Phys. 25 (1954) 493–500.

[18] H.K. Forster, N. Zuber, Growth of a vapor bubble in a superheated liquid, J. Appl. Phys. 25 (1954) 474–478.

[19] M.D. Donne, M.P. Ferranti, Growth of vapor bubbles in superheated sodium, Int. J. Heat Mass Transfer 18 (1975) 477–493.

[20] H.S. Lee, H. Merte, Spherical vapor bubble growth in uniformly superheated liquids, Int. J. Heat Mass Transfer 39 (1996) 2427–2447.

[21] C.A.J. Fletcher, Computational Techniques for Fluid Dynamics, second ed., Springer, New York, 1991, pp. 236–241.

[22] W. Wagner, A. Pruss, International equations for the saturation properties of ordinary water substance – revised according to the international temperature scale of 1990 (vol. 16, 1987, pp. 893), J. Phys. Chem. Ref. Data 22 (1993) 783–787.

[23] A.J. Robinson, R.L. Judd, The dynamics of spherical bubble growth, Int. J. Heat Mass Transfer 47 (2004) 5101–5113.

[24] K.E.J. Lehtinen, M.R. Zachariah, Energy accumulation in nanoparticle collision and coalescence processes, J. Aerosol Sci. 33 (2002) 357–368.

[25] M.F.M. Osborne, The acoustical concomitants of cavitation and boiling, produced by a hot wire. Part 2, J. Acoust. Soc. Am. 19 (1947) 21–29.

[26] Y.Y. Hsu, R.W. Graham, Transport Processes in Boiling and Two-Phase Systems, first ed., Hemisphere and McGraw-Hill, 1976.

[27] A. Esmaeeli, G. Tryggvason, Computations of film boiling. Part I. Numerical method, Int. J. Heat Mass Transfer. 47 (2004) 5451–5461.

[28] A. Prosperetti, A generalization of the Rayleigh–Plesset equation of bubble dynamics, Phys. Fluids 25 (1982) 409–410.